Nanoscale

Accepted Manuscript

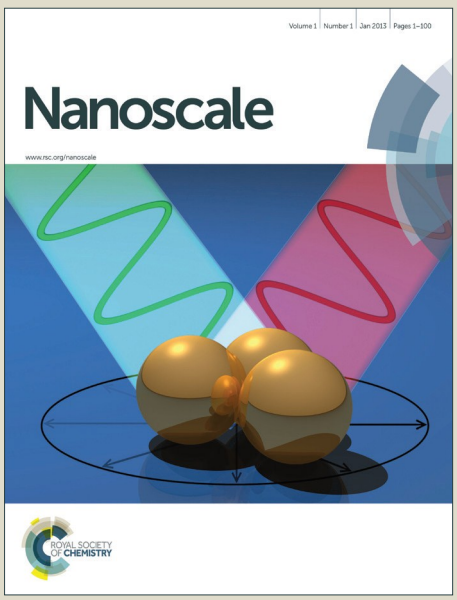

ROYAL SOCIETY OF CHEMISTRY

www.rsc.org/nanoscale

ARTICLE Journal Name

Preparing Non-volatile Resistive Switching Memories by Tuning the content of Au@air@TiO_2-*h* Yolk-shell Microspheres in Poly(3-hexylthiophene) Layer

Received 00th January 20xx,
Accepted 00th January 20xx

DOI: 10.1039/x0xx00000x

www.rsc.org/

Peng Wang, Quan Liu, Chun-Yu Zhang, Jun Jiang, Li-Hua Wang, Dong-Yun Chen, Qing-Feng Xu*, Jian-Mei Lu*

Crystalline hybrid microspheres, encapsulating a Au nanocore in the hollow cavity of a hairy semiconductor TiO_2 shell (Au@air@TiO_2-*h* microspheres) was prepared by using template-assisted synthetic methods. The as-prepared microspheres are dispersed into Poly(3-hexylthiophene) (P3HT) matrix and used as a memory active layer. The electrical rewritable memory effects of the Al/[Au@air@TiO_2-*h* + P3HT]/ITO sandwich devices can be effectively and exactly controlled by tuning the microsphere content in the electroactive layer. To clarify the switching mechanism, different component in the device, such as P3HT and microspheres, has been investigated respectively. And it was determined that the switching mechanism can be attributed to the formation and rupture of the oxygen vacancies filament. These results suggest that Au@air@TiO_2-*h* microspheres are capable of the potential high density date storage. In addition, this finding would provide important guidelines for the reproducibility of nanocomposite-based memory devices and is helpful to demonstrate the switching mechanism of these devices.

Introduction

As typical silicon-based flash memory devices has been approaching their physical limitations[1], the strong demand for next generation nonvolatile memory devices capable of high-density, low-power, easy-access and low misreading rate is driving a huge amount of research. Due to structure simplicity and high switching speed[2], resistance switching memory (RRAM) devices have been considered as potential candidates for nonvolatile memory.

Resistance material-based storage, including silicon[3-5], binary oxides[6-8], perovskite oxides[9-11] and organic materials[12-14], has been the subject of extensive research. Among them, titanium dioxide (TiO_2) is one of the most promising switching materials, which is widely used in electronic[15] and optoelectronic[16] applications, due to its easy fabrication, simple composition, and resistive switching properties. Its reversible switching is commonly attributed to the oxygen vacancy (ion) and the type of movement of oxygen vacancies are determined by the formation and rupture of conducting filaments or interface barrier modulation. As we known, Nanometer-scale materials-based devices, such as MoS_2 nanosheets[17] and graphene quantum dots[18], show higher performance than that of non-nanomaterials[19], but there is few report of TiO_2 nanoparticles (NPs)-based memory devices in literature. Therefore, research on TiO_2 NPs-based memory device will be a fresh and challenging task.

Yolk-shell nanomaterials with an interstitial space between the 'shell' and 'core' in a yolk-shell microsphere, have the potential to combine the individual properties of each component or achieve enhanced performance through cooperation between the components[20]. Recent studies show they may offer a promising application in memory materials. Reddy et al.[21] reported Al/Al_2O_3 yolk-shell NPs-based devices with multilevel conductance switching behavior and Ham et al.[22] reported the ON/OFF ratio for an InP-ZnS yolk-shell NPs-based device, which was significantly higher, with longer retention time, than devices without NPs. While displaying the capability of yolk-shell structures, the switching effects of these devices showed only WORM-type. Moreover, yolk-shell NPs are always referred as a unit when discussing their switching mechanism, inducing that the individual roles of 'core' and 'shell' in the NPs are still unclear, largely limiting the potential application of these devices. Thus, we postulate to fabricate a novel nanocomposite-based device that exhibits various switching effects, and the role of different component in the device can be distinguished.

In this paper, we design and synthesized a double-metal yolk-shell memory material (Au@air@TiO_2-*h* microspheres) under low temperature (45 ℃), encapsulating an Au nanocore in the hollow cavity of a hairy semiconductor TiO_2 shell. Combing Au and TiO_2 can takes advantage of both the dielectric properties[23] of Au and the versatile resistive switching properties[15] of TiO_2, and therefore provide a channel to achieve excellent electrical behavior. P3HT was chosen as the matrix[24, 25], due to its good chemical stability, high mobility, and low optical energy band gap. Interestingly, the rewritable switching behavior of the Al/[Au@air@TiO_2-*h* +P3HT]/ITO device can be effectively and precisely controlled by varying the Au@air@TiO_2-*h* content in the electroactive layer. Additionally, the roles of each component in this device were investigated. These may provide a new strategy for designing double-metal yolk-shell nanoparticles-based memory device materials and the demonstration of resistance switching in these devices are perhaps a key step toward the development of high-density sandwich RRAM.

Key Laboratory of Organic Synthesis of Jiangsu Province, College of Chemistry, Chemical Engineering and Materials Science, and Collaborative Innovation Center of Suzhou Nano Science and Technology, Soochow University, 199 Ren'ai Road, Suzhou 215123, China.
E-mail addresses: xuqingfeng@suda.edu.cn (Q.-F. Xu), lujm@suda.edu.cn (J.-M. Lu).
†Electronic Supplementary Information (ESI) available: [details of any supplementary information available should be included here]. See DOI: 10.1039/x0xx00000x

Fabrication and experiment methods

Materials

Hydrogen tetrachloroaurate trihlydrate ($HAuCl_4 \cdot 3H_2O$, 99%), tetraethyl orthosilicate (TEOS, 98%), polyvinylpyrrolidone(PVP, M_w=10,000 g/mol), trisodium citrate (≥99%), poly(3-hexylthiophene) (P3HT, 97%, M_w=40,000-70,000) and tetrabutyl orthotitanate (TBOT) were obtained from TCI Chem. Co. and were used as received without further purification. Ammonium hydroxide solution (13.2 m, Merck), alcohol and potassium hydroxide (KOH) were used as received without further purification.

Synthesis of Au NPs

Gold nanoparticles (Au NPs) were prepared according to Xia et al. and Li et al.[26, 27]. Briefly, 30 mL of aqueous solution of $HAuCl_4 \cdot 3H_2O$ (110 mg, 0.28 mmol) were added to a 50 mL round bottom glass flask and heated under reflux conditions. 4.1 mL of 5 wt % (0.695 mmol) fresh aqueous solution of trisodium citrate was added immediately. The reaction proceeded under reflux for 30 min. Stable Au NPs with an average diameter of 16 nm were obtained. Followed the mixture was cooled to ambient temperature. Approximately 4 mg PVP was added into the mixture to stabilize the Au NPs, and the resulting mixture was magnetically stirred for 24 h at room temperature. Afterwards, the Au NPs powder was separated from the solution by centrifuging at 6000 rpm for 10min and dispersed again in 50 µL ethanol.

Synthesis of Au@SiO_2 core-shell microspheres

The Au@SiO_2 core-shell microspheres were synthesized through a modified Stöber method[28]. The as-prepared Au NPs solution was dispersed in a mixture of deionized water (20 mL), ethanol (200 mL), and ammonia (28 wt%, 3mL). TEOS (1 mL) was subsequently added dropwise, and the reaction proceeded for 8 h under stirring. The Au@SiO_2 core-shell microspheres powder was separated from the solution by centrifuging at 6000 rpm for 10min, followed by washing with ethanol four times and then deionized water four times.

Synthesis of Au@SiO_2@TiO_2-*h* microspheres

The obtained Au@SiO_2 microspheres powder (0.4 g) were re-dispersed in absolute ethanol (250 mL), and mixed with ammonia solution (1.2 mL, 28 wt%) under ultrasound for 15 min. Afterwards, 2.6 mL of TBOT was added dropwise over 5 min, and the reaction was allowed to proceed for 30 h at 45℃ under mechanical stirring. The Au@SiO_2@TiO_2-*h* microspheres powder was separated from the solution by centrifuging at 6000 rpm for 10min, followed by washing with deionized water three times and then ethanol three times.

Synthesis of Au@air@TiO_2-*h* yolk-shell microspheres

The obtained Au@SiO_2@TiO_2-*h* yolk-shell microspheres (0.26 g) were added to an aqueous solution of KOH (80 mL, 0.2M) under mechanical stirring for 24 h at room temperature. The Au@air@TiO_2-*h* yolk-shell microspheres were centrifuged at 6000 rpm for 8 min, followed by washing with deionized wa 3 times and then ethanol 3 times. Finally, the anatase phas powder was obtained by drying at 60℃ under vacuu overnight.

Device fabrication and characterization

The electrical properties of the Au@air@TiO_2-*h* yolk-she microspheres were evaluated in Al/[Au@air@TiO_2-*h* +P3HT]/ITO thin-film sandwich devices. The ITO-gla substrates were pre-cleaned by ultrasonication for 20 min in deionized water, acetone, and alcohol, respectively. A 30µL tetrahydrofuran (THF)/ chlorobenzol (*v:v*=1:3) solution of P3H (20 mg/mL), containing 5, 12 or 20 wt% (relative to P3HT) the Au@air@TiO_2-*h* yolk-shell microspheres, was spin-coate onto the ITO-glass substrate, at a spinning speed of 1300 rpr for 1 min, to form the electroactive hybrid layer. The coate film was dried at room temperature overnight. The thickn of the electroactive polymer-microsphere composite layer was approximately 110 nm, as measured by a step-profiler. Fina the Al top electrode was deposited onto the film surface via thermal evaporation at 5 × 10^{-4} Pa through a shadow ma resulting in 0.4 × 0.4 mm^2 top electrodes approximately 20 nm thick. The devices were characterized under ambient conditions, using a KEITHLEY 4200-SCS-semiconducto characterization system.

Materials characterization

Field-emission scanning electron microscopy (FESEM) images were obtained on a Hitachi S-4200 SEM. Transmission electro microscopy (TEM) images were obtained on a Tecnai G220 TEM. The UV/Vis absorption spectra in the Wavelength rang of 300 to 700 nm were measured on Shimadzu UV-3600 spectrophotometer. X-ray diffraction (XRD) measuremen were carried out using a Rigaku CCD X-ray diffractometer with Ni-filtered $Cu_{K\alpha}$ radiation (40 kV, 40 mA).

Result and discussion

The Au@air@TiO_2-*h* yolk-shell microspheres were prepared by using template-assisted synthetic methods[29, 30]. As illustrated in Scheme 1a, the synthesis procedure of the NPs consists three main steps. First, as-prepared Au NPs were coated wit SiO_2 to obtain Au@SiO_2 yolk-shell microspheres. With th hydrolysis of TEOS, an approximately 50 nm thick SiO_2 laye was coated onto the Au particles (Fig. S1). The obtaine Au@SiO_2 microspheres exhibited a regular spherical shap with a smooth surface. Then, the TiO_2 shell was assembled o the surface of Au@SiO_2 NPs by using tempating method a 45℃. The average size of the Au@SiO_2@TiO_2-*h* microsphere is approximately 80 nm (Fig. 1b). Finally, hierarchica Au@air@TiO_2-*h* yolk-shell microspheres were obtained b etching SiO_2 in a 0.2M aqueous solution of KOH.

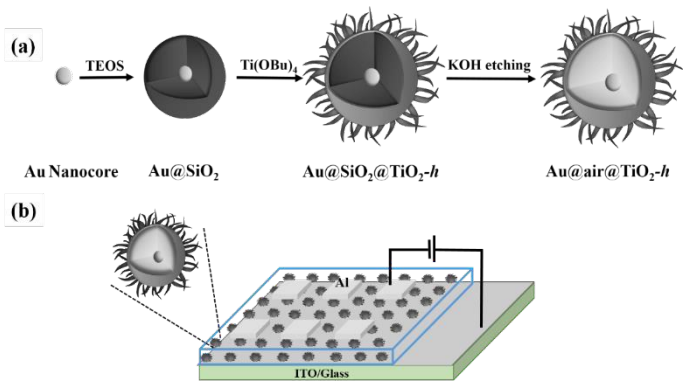

Scheme 1. (a) Schematic illustration of the synthesis of Au@air@TiO_2-*h* yolk-shell microspheres with an Au core and hairy TiO_2 shell; (b) the schematic diagram of the Al/[Au@air@TiO_2-*h* + P3HT]/ITO switching device.

Au NPs, Au@SiO_2, Au@ SiO_2@TiO_2-*h* and Au@air@TiO_2-*h* have been characterized by UV/Vis absorption spectra (Fig. S2) and X-ray diffraction (XRD) patterns (Fig. S3) (Detailed characterization was listed in supplementary information). TEM images further confirm that the yolk-shell structure is composed of an Au core approximately 16 nm in diameter, and well-defined TiO_2-*h* shell, about 13 nm in thickness (Fig. 1c and 1d).

To obtain uniform and consistent solid films, P3HT was selected as the matrix. FT-IR spectra of [Au@air@TiO_2-*h* + P3HT] composite and pure P3HT are shown in Fig. S4. It can be seen that the absorption band at 755 nm and 1376 nm is assigned to Ti-O vibration in TiO_2 and C-H vibration of CH_3 group in P3HT respectively, indicating that P3HT is integrated into the microspheres. For further research, the [Au@air@TiO_2-*h* + P3HT] films with different microspheres content were prepared. According to AFM results (Fig. S5), composite films with 5-20 wt% Au@air@TiO_2-*h* microspheres have a relatively smooth surface; the surface average roughness is less than 4 nm, indicating that Au@air@TiO_2-*h* microspheres have been uniformly distributed in the P3HT matrix. However, when the microsphere content in the films is increased to 30 wt%, the surface average roughness increased to more than 10 nm and failed to form the electroactive layer of the memory devices. Results indicate that the suitable polymer/nanoparticle ratio improves the surface uniformity and decreases the average roughness. Hence, in this paper, the typical MIM (metal-insulator-metal) structure devices containing 5 wt%, 12 wt% and 20 wt% Au@air@TiO_2-*h* microspheres were fabricated for the following research. A schematic view of the Au@air@TiO_2-*h* microspheres-based memory device is depicted in Scheme 1b, with the nanocomposite thin film sandwiched between the top Al electrode and bottom indium tin oxide (ITO) electrode. The electroactive films in the centre of the devices were spin-coated, while top metal electrodes were deposited via thermal evaporation.

The resistive switching characteristic observed from the characteristic current-voltage (*I-V*) curves of the Al/[Au@air@TiO_2-*h* +P3HT]/ITO devices with different yolk-shell ratios are shown in Fig. 2. *I-V* characteristics were measured under ambient conditions, with the top Al electrode grounded while a bias voltage was applied to the bottom IT. When the content of the Au@air@TiO_2-*h* microsphere in th hybrid matrix was gradually increased, different switchin behaviors appeared during the *I-V* test.

Fig. 2a shows the switching characteristics of the Al/[5 wt Au@air@TiO_2-*h* + P3HT/ITO] device. Initially, the current of the device increases slowly with applied negative voltage adde and shows a slight current hysteresis until the voltage reach to -2.4 V. At the threshold voltage of -2.4 V, the current increase from about 10^{-9} A to 10^{-7} A (Sweep 1). The device retains a lower resistance state in the forward and reverse sweep between 0 V and 5 V (sweep 2). Even after the power has bee turned off for two hours, the current does not return to th higher resistance state with applied voltage (sweep 3 an sweep 4), indicating nonvolatile behavior of the device. standard reference device with pure P3HT (no microspheres was prepared and this reference device shows an insu behavior[24] (Fig. S6). These results indicate that yolk-shell microspheres act as stable date-storage cells in the poly layer, and the device without microspheres cannot be used for application in memory device.

The *I-V* curves of the Al/[12 wt% Au@air@TiO_2-*h* P3HT/ITO] device displayed bistable electrical switchin behavior (Fig. 2b). When a voltage sweep was applied from 0 to -5 V, the device was initially at high resistance state (HRS As the negative bias was increased further, the memory device switched from the HRS to the low resistance state (LRS) at th threshold voltage of -2.7 V, as indicated by the abrupt increase of the current from 10^{-6} A to 10^{-2} A (sweep 1). This HRS-to-LR transition could serve as the "write" process. The device remained in LRS during subsequent application of the secon scan (sweep 2) performed. After turning off power for about 2 min, the device could be reprogrammed from HRS to LRS at -2.7 V again and the current was kept in the LRS (sweep 3 and sweep 4). The HRS could be further written to the LRS wh the voltage was applied again, indicating that the memory device is rewritable, and this behavior is characteristic of Dynamic-Random-Access-Memory (DRAM) devices. Compared

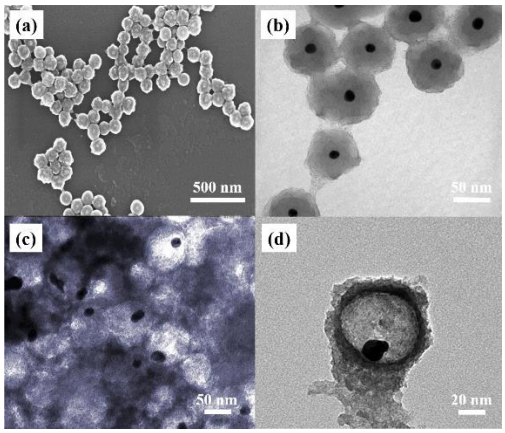

Figure 1. FESEM and TEM images of (a) (b) Au@SiO_2@TiO_2-*h* microspheres, (c) (d) Au@air@TiO_2-*h* microspheres. The respective scale bars for (a-d) are 500 nm, 50 nm 50 nm and 20 nm.

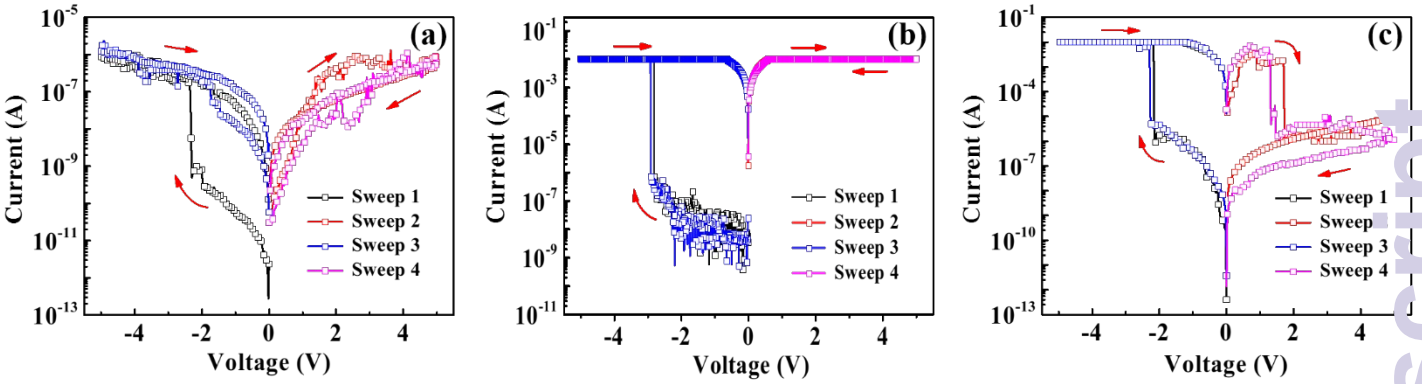

Figure 2. Typical current-voltage (*I-V*) characteristics of the Al/[Au@air@TiO_2-*h* + P3HT]/ITO switching device containing: (a) 5wt%, (b) 12 wt%, (c) 20 wt% Au@air@TiO_2-*h* microspheres. Compliance current (I_{cc}) is set as 10 mA during the test. (Electrode area =0.4 × 0.4 mm^2).

to the device with 5 wt% microspheres, the LRS/HRS current ratio is largely increased 100 times. This may result from higher microspheres content (＞10%) in the middle hybrid film, showing better conductive behavior.

With the content of the Au@air@TiO_2-*h* microspheres up to 20 wt% in the active layer, different result is shown during the typical *I-V* tests (Fig. 2c). In the first sweep from 0 to -5 V, the device initially exhibits a high resistance state. Then, a sharp transition in current is observed from the HRS to LRS at a switching threshold voltage of approximately -2 V (sweep 1). This HRS-to-LRS transition can be regarded as the "writing" process or SET process. Additionally, the device can be kept in LRS during the subsequent scan from -5 to 0 V (the "reading" process). However, the device can return to the original HRS at the switching threshold voltage (approximately 1.3 V) during the positive second sweep from 0 to 5 V (Sweep 2). Such LRS-to-HRS transition can be regarded as the "erasing" process or RESET process. Then, the device remains at HRS when scanning from 5 V to 0 V. These results show a completing "write-read-erase" cycle , which may arise from the inherent electrical behavior of the hollow nanomaterials[31]. The HRS can be switched to LRS and back to HRS again when a DC voltage is applied (sweep 3 and sweep 4), indicating that the memory device is rewritable and exhibits a typical flash memory characteristic.

Through the precise control of the LRS and HRS, the LRS/HRS current ratio (more than 10^4) in the present device is high enough to promise a low misreading rate. No significant degradation was observed in the device in LRS and HRS after 2.5 h during the continuous stress test (Fig. 3a), indicating the stability of the hybrid active layer. Furthermore, endurance tests were conducted at a reading DC bias voltage of 0.1 V and plotted SET/RESET distribution during 100 cycles. Writing and erasing operations (Fig. 3b) were performed by applying pulse signals of -3 V/100 ms and 2.5 V/100 ms, respectively. The measurement results suggest that excellent rewrite characteristics[32] are shown by the Al/[20wt% Au@air@TiO_2-*h* + P3HT]/ITO device.

In order to better understand the yolk-shell nanoparticles-based devices, Au NPs, Au@SiO_2 and Au@SiO_2@TiO_2-*h* micropsheres based memory devices are also fabricated and measured (Fig. S6). When mixed with different component in the electroactive films, the current ratio of LRS/HRS is $10^{1.5}$,10 10^2, respectively, which is much lower than that o Au@air@TiO_2-*h* microspheres based devices (≥ 10^4). Thus, w choose Au@air@TiO_2-*h* microspheres based devices f further study.

To clarify the mechanism of the bistable electrical switch behavior of the Al/[Au@air@TiO_2-*h* + P3HT]/ITO device, the impact of the polymer (P3HT) in the electroactive layer of t device is primo-studied. As pure P3HT in the electroactiv layer shows insulating behavior (Fig. S7), interactions between polymer and microspheres in the active layer may be first ke point in this system. Polymethyl methacrylate (PMMA), typical insulating polymer, was selected for comparison. A memory device based on [Au@air@TiO_2-*h* + PMMA] active

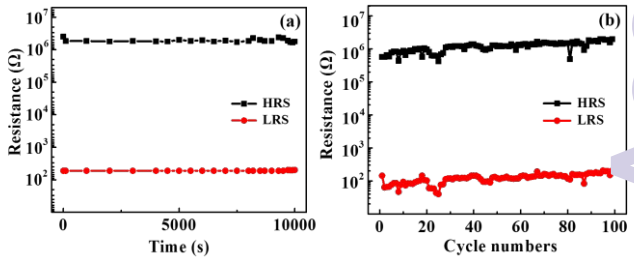

Figure 3. (a) Retention and (b) endurance properties of the Al/[20 wt% Au@air@TiO_2 + P3HT/ITO] device. The writing and erasing pulse are set to -3 V/100 ms and 2.5 V/100 ms, respectively, and a reading voltage of 0.1 V is applied.

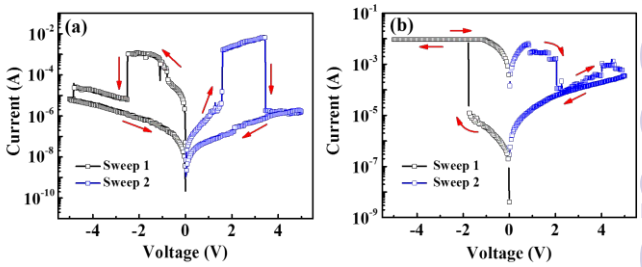

Figure 4. Typical current-voltage (*I-V*) characteristics of the (a) Al/[20 wt% Au@air@TiO_2-*h* + PMMA]/ITO ; (b) Au/[20 wt% Au@air@TiO_2-*h* + P3HT]/ITO switc device. (I_{cc} = 10 mA).

layer was prepared, and the *I-V* measurement is shown in Fig. 4a. The device is initially in HRS. When a DC voltage was applied from 0 V to -2.6 V, and from 0 V to 3.4 V, the current increases accordingly from HRS to LRS. However, at the voltage of -2.6 V and 3.4 V, the current occurred a sharp degradation from LRS to HRS, and kept the HRS with the subsequent reverse sweep. The results indicate that the PMMA-based device is not an ideal active material for memory performance. This may be attributed to the large energy gap (5.6 ev)[33] of PMMA, leading to electron transport among the PMMA matrix through the tunneling process[22], resulting in the formation of conductive filaments. When applying a high DC bias voltage, a large electronic current density is passed through the polymer layer, and the conductive filaments in the PMMA-based active layer may melt, causing a sharp decline in current[34]. According to the energy diagram for the Al/[Au@air@TiO_2-*h* + P3HT]/ITO device (Scheme 2), the energy gap of P3HT is approximately 2.1 eV[35]; the conduction band and valence band of TiO_2 are lower in energy than that of P3HT, indicating charges obtained from the electrode can easily transfer from P3HT to Au@air@TiO_2-*h* microspheres[36]. This suggests that the P3HT molecules would capture more electrons when a high DC bias voltage is applied, resulting in higher device conductivity and a more stable current curve during the test. Thus, P3HT are attributed to the device consists of Au@air@TiO_2-*h* microspheres and the device is more stable than the PMMA-based device under a large current.

To further understand the conduction process of Al/[Au@air@TiO_2-*h* + P3HT]/ITO device, the *I-V* curve fittings for the Al/[20% Au@air@TiO_2-*h* + P3HT]/ITO device in LRS and HRS are shown in Fig. 5. The HRS is characterized by the trap-limited space-charge-limited current (SCLC) model. The SCLC model (Fig. 5b) is comprised of three different conductive regions: (1) a transition region with a slope of 2.9, (2) a region shown a slight decrease to 2.6, and (3) a region marked by a sharp current increase, where the slope is approximately 4.5. In addition, LRS is dominated by the Ohmic model (Fig. 5a) and

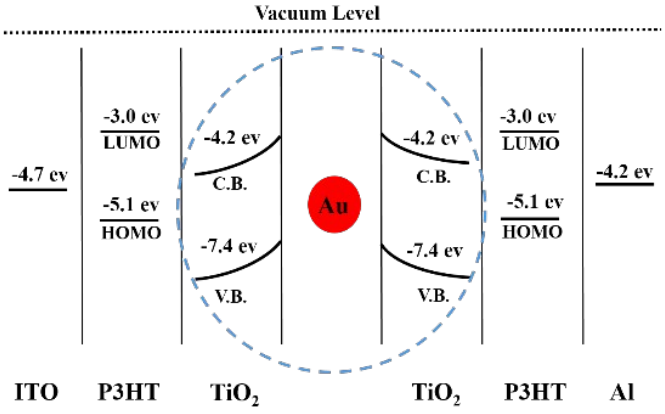

Scheme 2. The energy diagram relative to vacuum level for the Al/[Au@air@TiO_2-*h* + P3HT]/ITO switching device

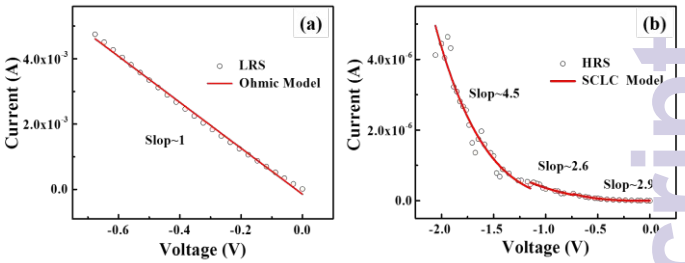

Figure 5. Experiment and fitted *I-V* characteristics of the Al/[Au@air@TiO_2-*h* + P3HT]/ITO device in (a) LRS and (b) HRS.

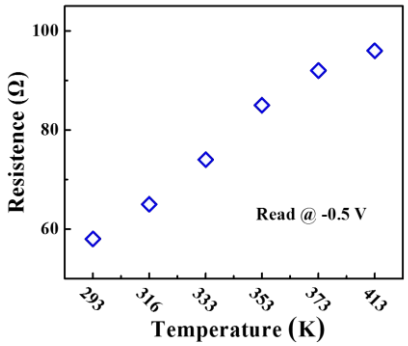

Figure 6. Temperature is dependent on resistance for the LRS under the read voltage of -0.5 V.

temperature-dependent resistance measurements for LRS states were also performed (Fig. 6). Interestingly, a conductive behavior was observed in the LRS measurement, that is, the resistance increasing as temperature increased. This indicates that the LRS is dictated by conductive filaments (CFs)[37]. Hence, results suggested that the conduction behavior of the RRAM is governed by SCLC and the formation of localized filament paths[38].

In order to further investigate the CFs in the Al/[Au@air@TiO_2-*h* + P3HT]/ITO device, Au is used as a top electrode to form an Au/[20 wt% Au@air@TiO_2-*h* + P3HT]/ITO memory device. The typical *I-V* curves of these memory cells were measured under a DC voltage sweep at room temperature (Fig. 4b). Although similar memory behavior is observed, there are some distinct differences that cannot be neglected. The current appears promotion at a voltage of around –1.7 V, and LRS/HRS current ratio, approximately 10^3, is slightly lower than that of devices using Al top electrode (10^4). This may be caused by the Al top metal's strong oxygen affinity[39]. As no great performance change occurs, therefore this behavior of Al metal does not critically affect the system. According to previous literature[38, 40], when electrons in the Al top electrode device transfers from the electrode to the microspheres, a redox reaction will be occurred to create mobile oxygen ions (O^{2-}) that can reversibly drift by external voltage biases during SET/RESET processes, resulting the forming of CFs.

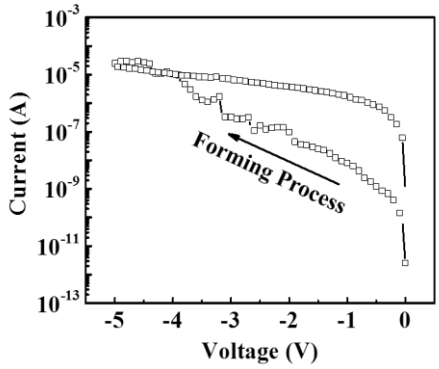

Figure 7. Typical current-voltage (*I-V*) characteristics of the Al/[12 wt% air@TiO_2-*h* + P3HT]/ITO switching device.

Finally, the impact of the Au core in the devices was studied. The electro-forming process of the Al/[12 wt% air@TiO_2-*h* + P3HT]/ITO device occurred with the application of an electrical bias ranging from 0 V to -5 V and the device retained the LRS with the subsequent reverse sweep (Fig. 7). As reported in literature[15, 40], the electrical switching effect maybe originate from the formation and rupture of the oxygen vacancies (V_O) filament. Comparing the results to that of the device containing Au@air@TiO_2-*h* NPs, we consider that the Au cores have some contribution during the electric test, that is, the filament path may be formed through the Au nanocores. Hence, we promote a probable switching mechanism of Al/[Au@air@TiO_2-*h* + P3HT]/ITO device.

The electrical switching mechanism of the Al/[Au@air@TiO_2-*h* + P3HT]/ITO devices can probably be attributed to the formation and rupture of the oxygen vacancy filament. The schematic diagram in Fig. 8a shows a widely recognized device. During the SET progress, the oxygen vacancies migrate from bottom electrode to top electrode under the negative DC bias as the case in Au@air@TiO_2-*h* microspheres. At a certain applied voltage, the generation of oxygen vacancies is triggered by the pre-existing Au nanocore defects because of the Au nanocore induced local electric field enhancement[41, 42]. When the voltage is sufficiently high, the defects align to form a vacancy path through the Au nanocore so a completely vacancy path is created, resulting the device transferring from HRS to LRS. Simultaneously, O^{2-} ions migrate when an electric field is applied, resulting in the creation of CFs through the microspheres, as shown in Fig 8b. Joule heating melts the CFs and the oxygen vacancy path dissolves simultaneously under the subsequent positive voltage, thus, the device switches back to the HRS, as shown in Fig. 8c, characteristic of the rewriteable behavior.

Therefore, from the above results, the devices with the different content of Au@air@TiO_2-*h* microspheres in the active layers showed different performance. The memory performance is unsatisfied with a very low content (5 wt%) of Au@air@TiO_2-*h* microspheres. This may attribute to the insufficient NPs, so that vacancy paths cannot be fully formed during the SET progress, inducing the decrease of performance. Consequently, with higher content, the better performance was obtained as sufficient vacancy paths formed.

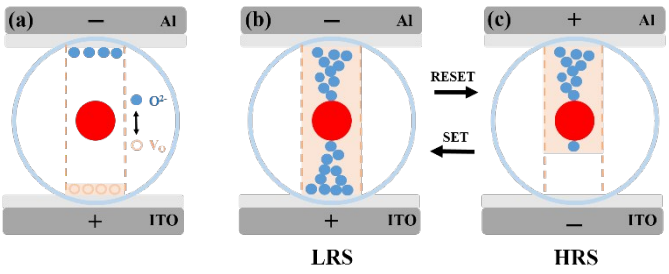

Figure 8. Schematic illustration of conductive filament formation and rupture of the Al/[Au@air@TiO_2-*h* + P3HT]/ITO device in LRS and HRS. (a) oxygen vacancy path containing Au nanocores, (b) metallic CF formed in the LRS, and (c) ruptured CF in the HRS of the electroactive layer. The red dots represent Au nanocores, cyan cycle represents TiO_2-*h* shell, blue dots represent oxygen ions, the pink region represents the oxygen vacancy path and the pink hollow spheres represent oxygen vacancies.

Conclusions

In summary, Au@air@TiO_2-*h* yolk-shell microspheres with a Au nanocore and anatase hairy TiO_2 shell were synthesized by using template-assisted synthetic methods. The obtained Au@air@TiO_2-*h* microspheres (~ 80 nm) can be uniformly integrated into P3HT thin films. Through controlling the microspheres content in the composite film, Al/[Au@air@TiO_2-*h* + P3HT]/ITO sandwich devices present long-term storage stability and exhibit rewriteable memory effects. According to physical models, the switching mechanism in the present device can be attributed to the formation and rupture of the oxygen vacancy filament through yolk-shell nanoparticles. Specifically, each Au@air@TiO_2-*h* microsphere can be treated as an independent memory cell, illustrating yolk-shell nanomaterials have excellent potential for high-density data storage at the nanoscale.

Acknowledgements

The authors graciously thank Pro. Jun-Wei Zheng from Soochow University for helpful discussion. The authors graciously thank the Chinese Natural Science Foundation (21371128 and 21336005), Qing-Lan project of Jiangsu and the major research project of Jiangsu Province office of Education (15KJA15008).

References

1. C. Cagli, F. Nardi, B. Harteneck, Z. Tan, Y. Zhang and D. Ielmini, *Small*, 2011, **7**, 2899-2905.
2. L. He, Z.-M. Liao, H.-C. Wu, X.-X. Tian, D.-S. Xu, G. L. Cross, G. S. Duesberg, I. V. Shvets and D.-P. Yu, *Nano letters*, 2011, **11**, 4601-4606.
3. G. Wang, A.-R. O. Raji, J.-H. Lee and J. M. Tour, *ACS nano*,

2014, **8**, 1410-1418.
4. L. Ji, Y.-F. Chang, B. Fowler, Y.-C. Chen, T.-M. Tsai, K.-C. Chang, M.-C. Chen, T.-C. Chang, S. M. Sze and E.-T. Yu, *Nano letters*, 2013, **14**, 813-818.
5. T.-M. Tsai, K.-C. Chang, T.-C. Chang, Y.-E. Syu, K.-H. Liao, B.-H. Tseng and S. M. Sze, *Applied Physics Letters*, 2012, **101**, 112906.
6. S. Seo, M. Lee, D. Seo, E. Jeoung, D.-S. Suh, Y. Joung, I. Yoo, I. Hwang, S. Kim and I. Byun, *Applied Physics Letters*, 2004, **85**, 5655-5657.
7. H. Shima, F. Takano, H. Muramatsu, H. Akinaga, Y. Tamai, I. H. Inque and H. Takagi, *Applied Physics Letters*, 2008, **93**, 113504.
8. X. Cao, B. Zheng, W. Shi, J. Yang, Z. Fan, Z. Luo, X. Rui, B. Chen, Q. Yan and H. Zhang, *Advanced materials*, 2015, **27**,4695-4701.
9. Y. Kim, K. Kook, S.-K. Hwang, C. Park and J. Cho, *ACS nano*, 2014, **8**, 2419-2430.
10. A. Bera, H. Peng, J. Lourembam, Y. Shen, X.-W. Sun and T. Wu, *Advanced Functional Materials*, 2013, **23**, 4977-4984.
11. A. Faraz, N. Deepak, M. Schmidt, M. E. Pemble and L. Keeney, *AIP Advances*, 2015, **5**, 087123.
12. B. Kam, X. Li, C. Cristoferi, E. C. Smits, A. Mityashin, S. Schols, J. Genoe, G. Gelinck and P. Heremans, *Applied Physics Letters*, 2012, **101**, 033304.
13. K. J. Baeg, D. Khim, J. Kim, B.-D. Yang, M. Kang, S.-W. Jung, I.-K. You, D.-Y. Kim and Y.-Y. Noh, *Advanced Functional Materials*, 2012, **22**, 2915-2926.
14. W. Ai, J. Jiang, J. Zhu, Z. Fan, Y. Wang, H. Zhang, W. Huang and T. Yu, *Advanced Energy Materials*, 2015, **5**, 1500559.
15. K. Kamiya, M. Young Yang, S.-G. Park, B. Magyari-Köpe, Y. Nishi, M. Niwa and K. Shiraishi, *Applied Physics Letters*, 2012, **100**, 073502.
16. S. Mubeen, G. Hernandez-Sosa, D. Moses, J. Lee and M. Moskovits, *Nano letters*, 2011, **11**, 5548-5552.
17. Z. Yin, Z. Zeng, J. Liu, Q. He, P. Chen and H. Zhang, *Small*, 2013, **9**, 727-731.
18. L. Kou, F. Li, W. Chen and T. Guo, *Organic Electronics*, 2013, **14**, 1447-1451.
19. J. Liu, J. Xu, R. Che, H. Chen, M. Liu and Z. Liu, *Chemistry*, 2013, **19**, 6746-6752.
20. J. Gu, Y. Guo, Y. Jiang, W. Zhu, Y.-S. Xu, Z.-Q. Zhao, J.-X. Liu, W.-X. Li, C. Jin and C.-H. Yan, *The Journal of Physical Chemistry C*, 2015, **119**, 17697-17706.
21. V. S. Reddy, S. Karak and A. Dhar, *Applied Physics Letters*, 2009, **94**, 173304.
22. J.-H. Ham, D.-H. Oh, S.-H. Cho, J.-H. Jung, T.-W. Kim, E.-D. Ryu and S.-W. Kim, *Applied Physics Letters*, 2009, **94**, 112101.
23. H.-C. Chang, C.-L. Liu and W.-C. Chen, *Advanced Functional Materials*, 2013, **23**, 4960-4968.
24. A. Prakash, J. Ouyang, J.-L. Lin and Y. Yang, *Journal of Applied Physics*, 2006, **100**, 054309.
25. K. K. Park, J.-H. Jung and T.-W. Kim, *Applied Physics Letters*, 2011, **98**, 193301.
26. H. Xia, S. Bai, J. r. Hartmann and D. Wang, *Langmuir : the ACS journal of surfaces and colloids*, 2009, **26**, 3585-3589.
27. X. Ji, X. Song, J. Li, Y. Bai, W. Yang and X. Peng, *Journal of the American Chemical Society*, 2007, **129**, 13939-13948.
28. J. Liu, J. Xu, R. Che, H. Chen, Z. Liu and F. Xia, *Journal of Materials Chemistry*, 2012, **22**, 9277-9284.
29. I. Lee, J.-B. Joo, Y. Yin and F. Zaera, *Angewandte Chemie*, 2011, **123**, 10390-10393.
30. J.-B. Joo, Q. Zhang, I. Lee, M. Dahl, F. Zaera and Y. Yin, *Advanced Functional Materials*, 2012, **22**, 166-174.
31. Q.-D. Ling, D.-J. Liaw, C. Zhu, D. S.-H. Chan, E.-T. Kang and K.-G. Neoh, *Progress in Polymer Science*, 2008, **33**, 917-978.
32. Y.-C. Chen, H.-C. Yu, C.-Y. Huang, W.-L. Chung, S.-L. Wu and Y.-K. Su, *Scientific reports*, 2015, **5**, 10022.
33. J. A. Hagen, W. Li, A. J. Steckl and J. G. Grote, *Applied Physics Letters*, 2006, **88**, 171109.
34. A. Suresh, G. Krishnakumar and M. A. G. Namboothiry, *Physical Chemistry Chemical Physics*, 2014, **16**, 13074-13077.
35. S. Lu, S.-S. Sun, X. Jiang, J. Mao, T. Li and K. Wan, *Journal of Materials Science: Materials in Electronics*, 2009, **21**, 682-686.
36. M.-Y. Chiu, C.-C. Chen, J.-T. Sheu and K.-H. Wei, *Organic Electronics*, 2009, **10**, 769-774.
37. H. Wang, Y. Du, Y. Li, B. Zhu, W.-R. Leow, Y. Li, J. Pan, T. Wu and X. Chen, *Advanced Functional Materials*, 2015, **25**, 3825-3831.
38. D.-H. Kwon, K.-M. Kim, J.-H. Jang, J.-M. Jeon, M.-H. Lee, G.-H. Kim, X.-S. Li, G. S. Park, B. Lee, S. Han, M. Kim and C. S. Hwang, *Nature nanotechnology*, 2010, **5**, 148-153.
39. H.-Y. Jeong, J.-Y. Lee, S.-Y Choi, *arXiv preprint arXiv:1007.2463*, 2010, 13.
40. H.-Y. Jeong, J.-Y. Lee and S.-Y. Choi, *Advanced Functional Materials*, 2010, **20**, 3912-3917.
41. W.-R. Chen, T.-C. Chang, J.-L. Yeh, S. M. Sze and C.-Y. Chang, *Applied Physics Letters*, 2008, **92**, 152114.
42. K. C. Park and S. Basavaiah, *Journal of Non-Crystalline Solids*, 1970, **2**, 284-291.